

29 *m*-xylene oxidation. Our results reveal that photochemical oxidation of *m*-xylene represents a
30 major source for SOA and BrC formation under urban environments, because of its large
31 abundance, high reactivity with OH, and high yields for COOs.

32 **Corresponding to:** Email: renyi-zhang@tamu.edu

33

34 **1. Introduction**

35 Photooxidation of anthropogenic and biogenic volatile organic compounds (VOCs)
36 produces tropospheric ozone, secondary organic aerosol (SOA), and brown carbon (BrC), with
37 profound implications for air quality, human health, and climate (Pope et al., 2002; Li et al., 2007;
38 IPCC, 2013; NASEM, 2016; Molina, 2021; Zhang et al., 2021). For example, SOA contributes to
39 the Earth energy budget, directly by scattering solar radiation and indirectly by serving as cloud
40 condensation nuclei to influence cloud formation and precipitation (IPCC, 2013; Wang et al., 2014;
41 Zhu et al., 2017). Also, light absorbing BrC interferes with solar radiation transfer, contributing to
42 positive radiative forcing (Wang et al. 2013; NASEM, 2016). VOC oxidation is initiated by various
43 oxidants (e.g., OH, O₃, NO₃, etc.) and proceeds via multiple pathways and stages (Atkinson, 2000;
44 Suh et al., 2001; Zhang et al., 2002; Zhao et al., 2004; Wennberg et al., 2018), yielding condensable
45 oxidized organics (COOs) to form SOA and BrC via gas-to-particle conversion (Finlayson-Pitts
46 and Pitts, 2000; Moise et al., 2015; Seinfeld and Pandis, 2016). Currently, the enormous chemical
47 complexity for VOC oxidation and gas-to-particle conversion represents one of the greatest
48 challenges in atmospheric chemistry research (Ravishankara, 1997; Zhang et al., 2015; NASEM,
49 2016). Aromatic hydrocarbons (e.g., benzene, toluene, xylenes, and trimethylbenzene) account for
50 20-30% of the total VOCs and are the major anthropogenic SOA precursors in the urban
51 atmosphere (Calvert et al., 2002; Ng et al., 2007; Song et al., 2007; Guo et al., 2014; Seinfeld and
52 Pandis, 2016). For example, *m*-xylene or C₆H₄(CH₃)₂ represents an important type of aromatic
53 hydrocarbons, which is emitted primarily from industrial and traffic sources. The concentration of

54 *m*-xylene ranges in a level from sub part per billion (ppb) up to several tens of ppb under urban
55 environments (Calvert et al., 2002; Fortner et al., 2009). Photooxidation of *m*-xylene is primarily
56 initiated by OH with a rate constant of $2.4 \times 10^{-11} \text{ cm}^3 \text{ molecule}^{-1} \text{ s}^{-1}$, which is nearly four times
57 higher than that of toluene (Fan and Zhang, 2008; Ji et al., 2017). A laboratory study identified *m*-
58 tolualdehyde, *m*-dimethylphenols, and dicarbonyls (i.e., glyoxal, methylglyoxal, unsaturated
59 dicarbonyls, and epoxy carbonyls) as the main gas-phase products from OH-initiated oxidation of
60 *m*-xylene (Zhao et al., 2005).

61 Several types of condensable oxidized organics (COOs) with distinct functionality and
62 volatility are produced from *m*-xylene photooxidation, contributing to aerosol nucleation and grow
63 (Zhang et al., 2004; Zhang et al., 2015; Guo et al., 2020). SOA formation is conventionally
64 considered to be mainly resulted from equilibrium gas-particle partitioning of semi-, intermediate-,
65 or low-volatile products (Shrivastava et al., 2017). Aromatic oxidation by OH yields low-volatile
66 polyhydroxy aromatics/quinones (denoted as PAQ hereafter), which condense to the aerosol-phase
67 (Schwantes et al., 2017). Also, chain autoxidation reactions of RO₂ from aromatics photooxidation
68 likely yield highly oxygenated molecules (HOMs) with low volatility (Molteni et al., 2018;
69 Garmash et al., 2020; Wang et al., 2020), although the reported yield of HOMs from *m*-xylene
70 oxidation is small (1.0-1.7%) (Molteni et al., 2018). Several key oxidation products of aromatic
71 oxidation have been shown to readily engage in multiphase reactions and contribute to SOA
72 formation (Ji et al., 2020, Li et al., 2021a). A recent experimental study demonstrated that SOA
73 formation from toluene photooxidation is mainly contributed by volatile dicarbonyls and organic
74 acids (Li et al., 2021b). Moreover, the aqueous reactions between small α -dicarbonyls and base
75 species (e.g., ammonia and amines) produce light-absorbing brown carbon (BrC) (De Haan et al.,
76 2011, 2017; Marrero-Ortiz et al., 2019; Li et al., 2021a,b). Previous experimental studies identified

77 the presence of hydroxy (C-OH), carbonyl (C=O), and acetal (C-O-C) functional groups in
78 aromatic-derived SOA formed via aqueous reactions, implicating a role of oxygenated organics in
79 SOA formation (Jia and Xu, 2014; Jia and Xu, 2018; Zhang et al., 2019). Also, laboratory
80 experiments showed that coating of *m*-xylene SOA on black carbon particles significantly
81 enhances scattering, absorption, and single scattering albedo (SSA) (Guo et al., 2016).

82 Current atmospheric models mainly parameterize SOA formation based on equilibrium
83 partitioning for semi- to low-volatile COOs (Shrivastava et al., 2017). However, gas-to-particle
84 conversion corresponds to decreasing entropy (i.e., $\Delta S \ll 0$), represents non-equilibrium chemical
85 processes (Peng et al., 2021). Moreover, the occurrence of particle-phase reactions significantly
86 alters the physiochemical properties (including volatility, hygroscopicity, and optical properties)
87 for COOs (Tan et al., 2012; Faust et al., 2017; Ji et al., 2020; Li et al., 2021a,b; Liu et al., 2021).
88 Notably, the volatility-based approach consistently under-predicts SOA formation (Heald et al.,
89 2005; Zhang et al., 2015; Hodzic et al., 2016), particularly during haze formation under polluted
90 conditions (Guo et al., 2014; Peng et al., 2021). Here we investigate the production of COOs with
91 different functionalities and assess their roles in SOA formation from *m*-xylene oxidation. A
92 primary objective of this work is to establish a functionality-based framework to predict SOA
93 formation from VOC photooxidation.

94 **2. Experimental Methodology**

95 **2.1 Chamber experiments**

96 The production of COOs and their roles in SOA formation from *m*-xylene oxidation were
97 investigated using a 1 m³ chamber (Teflon® PFA, Fig. S1 in the Supplementary Information or
98 SI), similar to our previous studies (Li et al., 2021a,b). The environmental chamber was equipped
99 with eighteen black light lamps (18 × 30W, F30T8/350BL, Sylvania). A water bubbler at a

100 temperature of 30°C was used to humidify the chamber to 10%, 30%, 50%, or 70% relative
101 humidity (RH), and all experiments were performed at 298 K. Three types of seed particles were
102 produced using a constant output atomizer (Model 3076, TSI) to represent various chemical
103 compositions, i.e., NH₄HSO₄ - ammonium bisulfate (ABS), (NH₄)₂SO₄ - ammonium sulfate (AS)
104 in the presence and absence of NH₃, and NaCl - sodium chloride. Seed particles were dried to RH
105 of ~2% by a Nafion drier (PD-070-18T-12SS, Perma Pure) and size-selected for an initial size of
106 100 nm by a differential mobility analyzer (DMA, Model 3081, TSI). Size-selected particles were
107 injected into the chamber with an initial particle concentration of $1.5 \times 10^4 \text{ cm}^{-3}$ measured by a
108 condensation particle counter (CPC, Model 3760A, TSI). The acidity of seed particles was
109 estimated using a thermodynamic model (Fountoukis and Nenes, 2007; Wang et al., 2018), with
110 the pH value of 3~5 in the presence of gaseous NH₃ and 0~1 in the absence of gaseous NH₃ for
111 (NH₄)₂SO₄, -0.5 for NH₄HSO₄, and 7 for NaCl. To investigate the effects of NH₃ and NO_x,
112 commercially available gaseous NH₃ (2000 ppm NH₃ in N₂) and NO₂ (500 ppm NO₂ in air) was
113 injected into the chamber with a flow of 100 sccm. 600 μL H₂O₂ (35 wt%, Sigma-Aldrich) and 10
114 μL *m*-xylene (99.5%, Sigma-Aldrich) were injected into a glass reservoir, which was then flushed
115 into the chamber by a 10 slpm flow from a pure air generator (Aadco 737-11, Aadco Inc.) for 10
116 min. The gases were then mixed by a fan inside the chamber. Once desired concentrations were
117 established, the black light lamps were turned on to initiate H₂O₂ photolysis to generate OH
118 radicals. The initial concentration for *m*-xylene and the steady-state concentration for OH were
119 estimated to be 1.9 ppm and $2.1 \times 10^6 \text{ molecules cm}^{-3}$, respectively (Fig. 1a). The experimental
120 conditions are summarized in Table 1.

121 2.2 Analytical instruments

122 The particle size growth, density, light scattering/absorption were simultaneously and
123 continuously monitored, after monodispersed seed particles were exposed to the products of *m*-
124 xylene-OH oxidation in the reaction chamber. A scanning mobility particle sizer (SMPS)
125 consisting of a DMA and a CPC was used to continuously measure the particle size growth factor,
126 $GF = D_p/D_0$, where D_p is the diameter after exposure and $D_0 = 100$ nm is the initial diameter. Note
127 both D_p and D_0 correspond to the dry particle diameter measured after passing through a Nafion
128 dryer (~2% RH). An aerosol particle mass analyzer (APM, Model 3600, Kanomax) was used to
129 derive the particle density throughout the experiments (Li et al., 2021b). The density for the SOA
130 materials (ρ_{SOA}) is calculated by,

$$\rho_{SOA} = \frac{\rho \times GF^3 - \rho_0}{GF^3 - 1} \quad (1)$$

131 where ρ and GF are measured particle density (g cm^{-3}) and growth factor at t (min), respectively.
132 ρ_0 is the initial density of seed particles. The uncertainty in the density measurements was
133 estimated to be $\pm 0.03 \text{ g cm}^{-3}$.

134 To measure the optical properties of exposed particles, a 1-slp flow from the chamber
135 was diluted by 4-slp N_2 and introduced into a commercial integrating nephelometer (TSI 3563)
136 and a home-built cavity ring-down spectrometer (CRDS) throughout the experiment. Light
137 scattering (b_{sca}) and extinction (b_{ext}) at 532 nm were determined by the nephelometer and CRDS,
138 respectively. The nephelometer was calibrated by comparing measured b_{sca} with b_{ext} from CRDS
139 when measuring ammonium sulfate particles with diameters of 100 nm, 150 nm, 200 nm, 250 nm,
140 and 300 nm. The absorption coefficient (b_{abs}) was determined from ($b_{\text{ext}} - b_{\text{sca}}$), and SSA was
141 calculated from $b_{\text{sca}}/b_{\text{ext}}$.

142 The ID-CIMS using the hydronium reagent ion (H_3O^+) was employed to analyze gaseous
143 concentrations with a sample flow rate of 0.5 slpm from the chamber. The sample line was heated

144 to 70°C to reduce wall loss. Gas-phase concentrations of *m*-xylene and its oxidation products were
145 quantified by ID-CIMS. Briefly, the concentration of species A from the proton transfer reaction
146 ($\text{H}_3\text{O}^+ + \text{A} \rightarrow \text{H}_2\text{O} + \text{HA}^+$) is determined by,

$$[\text{A}] = \frac{S_{\text{A}}}{k_{\text{PTR}} \times \Delta t \times S_{\text{RI}}} \quad (2)$$

147 where S_{A} and S_{RI} are the mass spectrum intensities for A and reagent ions, respectively. k_{PTR} is the
148 proton-transfer rate constant between A and H_3O^+ (Zhao and Zhang, 2004). $\Delta t = \frac{l}{U_i}$ is the retention
149 time of ions, which is determined by the length of the drift tube $l = 8$ cm and the ion drift velocity
150 U_i . The ion drift velocity U_i is determined from:

$$U_i = u_0 \left(\frac{760 \text{ torr}}{p} \right) \left(\frac{T}{273 \text{ K}} \right) E \quad (3)$$

151 where $u_0 = 2 \text{ cm}^2 \text{ V}^{-1} \text{ s}^{-1}$ is the reduced ionic mobility (Dotan et al., 1976), $p = 3.0$ torr, $T = 298$ K,
152 and $E = 133 \text{ V cm}^{-1}$ is the voltage gradient in the drift tube. Alternatively, the concentrations of *m*-
153 xylene, dicarbonyls, and organic acids were also calibrated by preparing the vapors of *m*-xylene,
154 methylglyoxal with known mixing ratios in N_2 , and using a permeation tube of propanoic acid,
155 respectively (Li et al., 2021a). The detection limit (defined as 3 times of the ratio of signal to noise)
156 for the oxidation products from *m*-xylene-OH reactions was estimated to be 50 ppt by the ID-
157 CIMS.

158 The steady-state OH concentration was determined by exponential fitting ($y = ke^{-bx}$) of
159 the decay of *m*-xylene concentration (Fig. 1a),

$$[\text{OH}] = \frac{b}{k_1} \quad (4)$$

160 where $k_1 = 2.4 \times 10^{-11} \text{ cm}^3 \text{ molecule}^{-1} \text{ s}^{-1}$ is the second-order rate constant for *m*-xylene-OH
 161 oxidation (Fan and Zhang, 2008). The estimated concentration of OH was $2.1 \times 10^6 \text{ molecules cm}^{-3}$
 162 ³ in our experiments.

163 We also estimated loss of condensable vapors to the chamber wall using the first-order
 164 wall-loss coefficient, $k_w \text{ (s}^{-1}\text{)}$, by considering gas-phase transport within the chamber (Zhang et
 165 al., 2014)

$$k_w = \left(\frac{A}{V}\right) \frac{\alpha_w \bar{c}}{4 + \frac{\pi}{2} \left(\frac{\alpha_w \bar{c}}{\sqrt{k_e D_g}}\right)} \quad (5)$$

166 where A/V is the surface to volume ratio of the chamber (equal to $6/L$ for a square chamber, where
 167 $L = 1 \text{ m}$ is its dimension), α_w is the mass accommodation coefficient of vapors onto Teflon chamber
 168 walls, \bar{c} is the mean thermal speed of the molecules, k_e is the coefficient of eddy diffusion, which
 169 is estimated to be 0.5 based on the loss rate of particles (McMurry and Rader, 1985),

$$k_e = \frac{\left(\frac{\pi L \beta_0}{12}\right)^2}{D_b} \quad (6)$$

170 where β_0 is the fractional loss rate of particles,

$$\beta_0 = \frac{\Delta N}{N \times \Delta t} = \frac{15000 \text{ cm}^{-3} - 7500 \text{ cm}^{-3}}{15000 \text{ cm}^{-3} \times 7200 \text{ s}} = 1.4 \times 10^{-5} \text{ s}^{-1} \quad (7)$$

171 where N is the particle number concentration, $D_b = 6.75 \times 10^{-10} \text{ m}^2 \text{ s}^{-1}$ is the Brownian diffusion
 172 coefficient for particles. D_g is the gas-phase diffusion coefficient. For NH_3 , the mass
 173 accommodation coefficient of vapors onto the chamber wall is 0.05 (Zhang et al., 2014). Gas-
 174 phase diffusion constant D_g is $1.98 \times 10^{-5} \text{ m}^2 \text{ s}^{-1}$. The mean thermal speed \bar{c} is 603 m s^{-1} . The first-
 175 order wall-loss coefficient of NH_3 was calculated to be $1.2 \times 10^{-2} \text{ s}^{-1}$.

176 The average concentration of NH_3 or NO_x (noted as X) is estimated by,

$$\overline{[X]} = \frac{(1 - e^{-k_w \times \Delta t_i})}{k_w \times \Delta t_i} [X]_0 \quad (8)$$

177 For initial injection of 400 ppb NH₃, the average concentration of NH₃ was estimated to be 19 ppb.
178 The first-order wall-loss rate of NO_x was measured to be 2.5 × 10⁻³ h⁻¹, leading to negligible wall-
179 loss (Qi et al., 2020).

180 The particle-phase chemical composition was analyzed by thermal desorption (TD) - ID -
181 CIMS (TD-ID-CIMS) (Wang et al., 2010). Seed particles after 20 min of exposure to
182 photooxidation were collected for 2 hours by a platinum filament (with a collection voltage of
183 about 3000 V) in a 2.5 slpm flow from the reaction chamber, and the analytes were evaporated by
184 heating the filament to 350°C for 2 s and detected by ID-CIMS using H₃O⁺ as the reagent ions.
185 The mass resolution of TD-ID-CIMS was about 0.5 amu. The desorption signal was represented
186 by the relative intensity (RI) of the integrated peak area during heating. The uncertainties of TD-
187 ID-CIMS measurements arose from the flow rate, voltage, collection time, evaporation voltage,
188 and mass spectrometer ionization/detection efficiencies during particle collection and were
189 represented by the standard deviation of three repeated measurements. In both ID-CIMS and TD-
190 ID-CIMS configurations, an ion drift-tube was used. An electric field of E/N = 138 Td was applied
191 for ID-CIMS at high RH (i.e., 70%), and E/N = 110 Td was used for TD-ID-CIMS at low RH (<
192 1%). Formation of cluster ions was effectively suppressed, since a uniform electrical field in the
193 drift tube decomposed weakly-bonded cluster ions. Fragmentation using ID-CIMS or TD-ID-
194 CIMS was minimal, and all gaseous and particle-phase products were detected at their respective
195 parent-peaks, indicating little dissociation effect from either thermal desorption or ionization by
196 H₃O⁺ (Yuan et al., 2017). For example, the major molecules detected by TD-ID-CIMS at high RH
197 from *m*-xylene oxidation were acetal/hemiacetal oligomers, consistent with a previous study
198 showing intact oligomers with thermal desorption (Claflin and Ziemann, 2019).

199 While the gaseous concentrations of the oxidation products, GF, SSA, and density were
 200 temporally resolved in our experiments, the particle chemical composition reflected an overall
 201 aerosol chemical makeup during an experiment. To assess the effects of different seed particles,
 202 RH, and NH₃ on SOA and BrC formation, we compared the measured GF and SSA values after
 203 120-min exposure to the *m*-xylene-OH oxidation.

204 2.3 Uptake coefficient (γ) determination

205 The uptake coefficient (γ) for COOs is calculated by,

$$\gamma = \frac{4 \times FR \times kp}{\bar{c} \times S} \quad (9)$$

206 where *FR* is the percent contributions of the COO species from *m*-xylene-OH oxidation to the
 207 particle-phase mass intensity measured by TD-ID-CIMS. *kp* is measured first-order particle uptake
 208 rate constant for COOs (i.e., glyoxal, methylglyoxal, γ -dicarbonyls, organic acids, PAQ, and
 209 nitrophenols), which is calculated from the measured growth rate of seed particles,

$$kp = \frac{\pi \times (D_p^3 - D_0^3) \times \rho \times \bar{N} \times N_A}{6 \times MW \times [A] \times \Delta t} \quad (10)$$

210 where D_p and D_0 are the final and initial diameters of the particles during the time-period of,
 211 respectively, ρ is the density of total SOA, $\bar{N} = 11250 \text{ cm}^{-3}$ is the average particle number
 212 concentration during 120 min, $\Delta t = 120 \text{ min}$ is the exposure time, N_A is Avogadro constant, MW
 213 is the molar weight of species A, and $[A]$ is the average gas phase concentration of species A. \bar{c} is
 214 the mean thermal speed of A. S is the average surface area of aerosols ($\text{cm}^2 \text{ surface/cm}^3 \text{ air}$) during
 215 the period of $\Delta t = 120 \text{ min}$,

$$S = \frac{\pi \int_{t=0}^{120 \text{ min}} D^2 \times HGf^2 \times \bar{N} dt}{\Delta t} \quad (11)$$

216 where D is the time-dependent particle diameter, HGf is the hygroscopic growth factor of particles
 217 (Seinfeld and Pandis, 2016). The error bars of reactive coefficients are derived from the
 218 propagation of uncertainties for the parameters in eqs. 9-11 (i.e., 1 σ of at least three repeated
 219 measurements for each parameter).

220 2.4 Simulation of gaseous oxidation products

221 The gas-phase concentration of *m*-xylene-OH oxidation products were simulated by a tri-
 222 exponential kinetic model to account for the gas-phase oxidation, chamber wall loss, and particle
 223 uptake. The precursor A with an initial concentration of $[A]_0$ undergoes multiple steps of oxidation
 224 to yield multi-generation products, P_n (where $n = 1, 2, 3, \dots$). Once formed, each product engages
 225 in further oxidation with a pseudo first-order rate constant of $k'_{n+1} = k_{n+1}[\text{OH}]_{\text{ss}}$, particle uptake
 226 with a rate of kp_n , and wall loss with a rate of kw_n . The forward rate constants, k_{n+1} , were taken
 227 from MCM 3.3.1 (Jenkin et al., 2003). The rate of uptake kp_n is expressed by,

$$kp_n = \frac{1}{4} \gamma_n \bar{c} S \quad (12)$$

228 and the first-order wall loss rate constants were estimated by eq. 5 with the mass accommodation
 229 coefficients α_w constrained by the measured time-dependent concentration. The gas-phase
 230 concentrations of P_1 to P_3 are calculated by,

$$[P_1] = \frac{k'_1[A]_0}{k'_2 + kw_1 + kp_1 - k'_1} (e^{-k'_1 t} - e^{-(k'_2 + kw_1 + kp_1)t}) \quad (13)$$

$$[P_2] = C_1 e^{-(k'_3 + kw_2 + kp_2)t} + C_2 e^{-k'_1 t} - C_3 e^{-(k'_2 + kw_1 + kp_1)t} \quad (14)$$

$$[P_3] = C_4 e^{-(k'_4 + kw_3 + kp_3)t} + C_5 e^{-(k'_3 + kw_2 + kp_2)t} \\ + C_6 e^{-k'_1 t} - C_7 e^{-(k'_2 + kw_1 + kp_1)t} \quad (15)$$

231 where C_1 to C_7 are constants, and k'_n denotes the pseudo-first order rate constant,

$$k'_n = k_n[\text{OH}] \quad (16)$$

232 The rate constants and values for C₁ to C₇ are summarized in Table S1.

233 2.5 COO yield

234 The COO yield (Y_{COO}) from *m*-xylene oxidation is determined from,

$$235 Y_{\text{COO}} = [\text{COO}_i] / \Delta[\text{C}_6\text{H}_4(\text{CH}_3)_2] \quad (17)$$

236 where i represents the type of COO species, and $\Delta[\text{C}_6\text{H}_4(\text{CH}_3)_2]$ denotes the concentration of *m*-
237 xylene consumed due to OH oxidation. There were four types of COOs identified from our
238 experiments, i.e., dicarbonyls for $i = 1$, carboxylic acids for $i = 2$, PAQ for $i = 3$, and nitrophenols
239 for $i = 4$. The measured gaseous concentration for each COO is corrected for wall-loss and
240 unreacted earlier generation products,

$$[\text{COO}_i] = \{[\text{COO}_{i,f}] + (\frac{1}{4}\gamma_i\bar{c}S + kw_i)\overline{[\text{COO}_i]}\Delta t\} / (1 - \frac{[A_f]}{[A_t]}) \quad (18)$$

241 where $[\text{COO}_{i,f}]$ and $\overline{[\text{COO}_i]}$ are the final and time-averaged gas-phase concentrations of COO_{*i*} at
242 120 min, respectively. $[A_f]$ and $[A_t]$ are the unreacted and the total production of the earlier
243 generation species A, respectively.

244 2.6 SOA mass concentration and yield

245 The measured SOA mass concentration is calculated based on the aerosol size growth and
246 density,

$$M_{\text{SOA,meas.}} = \frac{1}{6}\pi(D_p^3 \times \rho_t - D_0^3 \times \rho_0) \times \bar{N} \quad (19)$$

247 where ρ_t and ρ_0 are the final and initial particle density during 120 min, respectively.
248 Alternatively, by categorizing COOs in accordance with the functional groups, we established a
249 framework to predict SOA formation from the measured production and reactivity. The SOA mass
250 concentration (M_{SOA}) is predicted from the measured uptake coefficients and average gas-phase
251 concentrations of COOs,

$$M_{SOA} = \sum_i^4 \frac{1}{4} \gamma_i \bar{c}_i S [A_i] MW_i \quad (20)$$

252 where MW_i is the molar weight of species i . γ_i is averaged over all identified species for each type
 253 (i) of COOs, and $[A_i]$ is the sum of the measured concentrations of all identified species for type i
 254 (time-averaged). The SOA mass yield is expressed by,

$$255 \quad Y_{SOA} = M_{SOA} / \{ \Delta [C_6H_4(CH_3)_2] \times MW_m \} \quad (21)$$

256 where MW_m is the molar weight of m -xylene.

257 To compare the measured and predicted SOA formation at RH = 10% and 70%, we
 258 corrected the increased vapor wall loss and reduced particle surface area at RH = 70% compared
 259 to 10% RH. A correction factor is determined from the average measured gas concentration ratios
 260 (R_c) between 10% and 70% RH for each type of COOs. Additionally, a hygroscopic volume
 261 enhancement factor (HVE) of 1.2 between 10% and 70% RH is adopted. The RH-corrected SOA
 262 mass for each COO is estimated by,

$$M_{i,corr} = R_c \times M_{SOA} \times \frac{S_1}{S_2} \times HVE \quad (22)$$

263 where S_1 and S_2 are the particle surface areas at 10% and 70% RH, respectively.

264 **3. Results and Discussions**

265 **3.1 Evolution of oxidation products**

266 To elucidate the production of COOs, we measured time-dependent gaseous concentrations
 267 of m -xylene oxidation products. The OH- m -xylene reactions occur via dominantly OH-addition to
 268 the aromatic ring to yield m -xylene-OH adducts and minorly H-abstraction from the methyl group
 269 to form methylbenzyl radicals (about 4%) (Fan and Zhang, 2008). The m -xylene-OH adducts then
 270 react with O_2 to form dimethylphenol via H-extraction or OH- m -xylene- O_2 peroxy radicals (RO_2)
 271 via O_2 addition (Fig. S2a). While the m -xylene mixing ratio exhibits an exponential decay

272 throughout the experiments (Fig. 1a), the formation of the gas-phase oxidation products follows
273 the rate-determining steps involving successive OH-oxidation with three major generations (Fig.
274 1b-e). The first-generation products (P_1) include dimethylphenol ($m/z = 123$) and
275 methylbenzaldehyde ($m/z = 121$), corresponding to OH addition to the aromatic ring (~96%) and
276 hydrogen extraction (~4%) from the methyl group, respectively (Fan and Zhang, 2008; Li et al.,
277 2021b). The second-generation products (P_2) mainly consist of methylglyoxal ($m/z = 73$),
278 methylbutenedial ($m/z = 99$), toluic acid ($m/z = 137$), and dimethylresorcinol (Fig. 1f and Fig. S2b),
279 which are produced from the P_1 reactions with OH/ HO_2 . For example, methylglyoxal and
280 methylbutenedial are formed from OH oxidation of dimethylphenol and subsequent ring-
281 opening or from the primary peroxy radical. The latter undergoes cyclization to form the bicyclic
282 radical, which then reacts with O_2 to form the secondary peroxy radical, followed by reactions
283 with HO_2 and subsequent ring-cleavage (Fan and Zhang, 2008). The third-generation products (P_3)
284 contain mainly multi-functional organic acids, including pyruvic acid ($m/z = 89$), 4-oxo-2-
285 pentenoic acid ($m/z = 115$), and 3-methyl-4-oxo-2-pentenoic acid ($m/z = 129$) produced from the
286 subsequent reactions of dicarbonyls with OH. Note that P_n in Fig. 1b denotes the lumped product
287 of the n^{th} generation, which is related the sequence of OH addition for *m*-xylene oxidation and
288 accounts for the various species detected by ID-CIMS (Fig. S2b).

289 The P_1 concentrations rise immediately upon initiating photooxidation and reach the peak
290 mixing ratios of about 20 ppb for dimethylphenol and 9 ppb for methylbenzaldehyde. There is a
291 slight decline in P_1 concentrations after 70 to 100 mins, reflecting their consumption from further
292 OH oxidation (Fig. 1c). The P_2 concentrations follow those of P_1 (Fig. 1d and Fig. S3a) and reach
293 the peak mixing ratios ranging from 0.4 to 2.4 ppb, dependent on their subsequent oxidation by
294 OH as well as loss to the chamber wall and aerosols. Note that the concentration of toluic acid

295 rises later than those of the dicarbonyls, attributable to the slower rates for H-abstraction by OH
296 from the methyl group than OH-addition to the aromatic ring (Fan and Zhang, 2008). The P₃
297 concentrations increase monotonically after a delay of 10-20 mins and reach a mixing ratio from
298 sub-ppb to 2.5 ppb at 120 min (Fig. 1e and Fig. S3b). The initial concentration of *m*-xylene (e.g.,
299 1940 ppb) in our experiment is higher than that in the atmosphere, potentially inducing self- and
300 cross-reactions of RO₂ to form alkoxy radicals (RO) or dialkyl peroxides (ROOR') leading to
301 HOMs. However, negligible products relevant to HOMs were detected in our experiments,
302 indicating a minor importance for the self- and cross-reactions of RO₂ compared to the competing
303 reactions between RO₂ and HO₂/NO/RO₂ to form ring-opening products. Our results for
304 insignificant contribution of HOMs to SOA formation from *m*-xylene oxidation are consistent with
305 a small yield of HOMs reported in a previous study (Molteni et al., 2018).

306 We simulated the time-dependent evolution of the gaseous products by employing a tri-
307 exponential kinetic model (Fig. 1b and Table S1). Multi-generation oxidation of *m*-xylene occurs
308 via consecutive reaction steps to produce a multi-generation product, P_{*n*} (where *n* denotes the
309 sequence of OH oxidation), which subsequently engages in additional OH oxidation, wall loss,
310 and aerosol loss. Fig. 1b-d indicates that the simulated concentrations well reproduce those
311 measured for P₁ to P₃ by adopting our measured γ (to be discussed below) and estimated wall loss
312 rates (see Methods and Table S1 in SI).

313 **3.2 Particle size growth, SSA, and chemical speciation**

314 To evaluate SOA and BrC formation from COOs, we measured the time-dependent GF,
315 SSA, and density, after (NH₄)₂SO₄ seed particles are exposed to the *m*-xylene oxidation products
316 in the presence of 19 ppb NH₃ and at 70% RH (Fig. 2a-c, Exp. 1). The GF increases monotonically
317 and reaches a value of (2.41 ± 0.03) at 120 min (Fig. 2a), while the SSA declines steadily

318 throughout the exposure and reaches the value of (0.91 ± 0.01) at 120 min (Fig. 2b). The latter is
319 indicative of the production of light-absorbing BrC. The measured SSA for *m*-xylene is lower than
320 that previously reported for toluene under comparable experimental conditions (Li et al., 2021b).
321 The difference in SSA/BrC formation between toluene and *m*-xylene is explained by a higher yield
322 of methylglyoxal from *m*-xylene than from toluene (Jenkin et al., 2003; Nishino et al., 2010), since
323 methylglyoxal produces BrC more efficiently via aqueous reaction than glyoxal (Li et al., 2021a).
324 Analysis of particle chemical composition using TD-ID-CIMS reveals high abundances of
325 oligomers, nitrogen-containing organics (NCO) consisting of N-heterocycles/N-heterochains,
326 carboxylates, along with a small amount of dimethylresorcinol/benzoquinone (Fig. 2c). The
327 identified mass peaks are summarized in Tables S2 to S4. Assuming similar sensitivity to proton-
328 transfer reactions for the aerosol-phase organics, i.e., with the proton transfer reaction rate
329 constants of $(2 \text{ to } 4) \times 10^{-9} \text{ cm}^3 \text{ molecule}^{-1} \text{ s}^{-1}$ (Zhao and Zhang, 2004), the contributions of
330 oligomers, NCO, carboxylates, and dimethylresorcinol/benzoquinone to the total SOA formation
331 are estimated to be 22%, 23%, 47%, and 8%, respectively, at 70% RH (Table S5). Note that the
332 TD-ID-CIMS method preserves the identify for all organic species without fragmentation,
333 providing unambiguous chemical speciation for the aerosol-phase products.

334 **3.3 Effects of seed particles, NH₃, RH, and NO_x**

335 We assessed the dependence of SOA/BrC formation from *m*-xylene-OH oxidation on
336 different seed particles (Exp. 1-4), NH₃ concentration (Exp. 1-12), RH (Exp. 1,13-15), and NO_x
337 concentration (Exp. 1,16-18). Fig. 3a shows that (NH₄)₂SO₄ in the presence of 19 ppb NH₃ exhibits
338 the largest GF and lowest SSA at 120 min, which are explained by the chemical mechanisms
339 leading to the formation of the observed aerosol-phase products. While dicarbonyls undergo
340 aqueous phase reactions to form oligomers (Fig. S4) (Ji et al., 2020; Li et al., 2021a), organic acids

341 engage in ionic dissociation and acid-base reaction to yield carboxylates (Fig. 3b). In addition, the
342 reaction of dicarbonyls with NH_3 produces N-heterocycles/N-heterochains (Fig. S5), which are
343 light-absorbing (Marrero-Ortiz et al., 2019; Li et al., 2021a). Oligomerization of dicarbonyls
344 involves protonation, hydration, and deprotonation, which are mediated by carbenium ions via
345 nucleophilic addition (Ji et al., 2020; Li et al., 2021a). While protonation of dicarbonyls to yield
346 carbenium ions is promoted by hydrogen ion activity, high acidity hinders hydration and
347 deprotonation, explaining the largest GF and the smallest SSA on weakly acidic $(\text{NH}_4)_2\text{SO}_4$
348 particles in the presence NH_3 (Fig. 3a). In addition, uptake of dicarbonyls, organic acids, and PAQ
349 is likely facilitated on aqueous $(\text{NH}_4)_2\text{SO}_4$ particles, because of surface propensity of charge-
350 separation at the interface (Hua et al., 2011; Shi et al., 2020). Specifically, surface-abundant NH_4^+
351 cations arising from interfacial charge separation of $(\text{NH}_4)_2\text{SO}_4$ likely exert electrostatic attraction
352 to gaseous oxygenated species (with a negative charge character) to enhance uptake for
353 dicarbonyls, organic acids, and PAQ (Li et al., 2021a,b). The most efficient formation of SOA and
354 BrC on $(\text{NH}_4)_2\text{SO}_4$ particles in the presence of NH_3 are also consistent with the measured highest
355 intensities for oligomers and NCO (Fig. 3b). On the other hand, ionic dissociation and acid-base
356 reaction to yield carboxylates occur efficiently in the presence of NH_3/NaCl , as evident from the
357 increasing carboxylate intensity from NH_4HSO_4 to NaCl (Fig. 3b). The GF and SSA increase and
358 decrease, respectively, with NH_3 from 0 to 27 ppb for all three types of seed particles (Fig. 4a,b),
359 relevant to the reactions of NH_3 with dicarbonyls to form NCO and with organic acids to form
360 ammonium carboxylates. The analysis of the particle composition confirms that the intensities of
361 oligomers, NCO, and carboxylates increase with the NH_3 concentration (Fig. 4c-e).

362 We carried out additional experiments by varying RH from 10% to 70% in the presence of
363 19 ppb NH_3 (Fig. 5). The GF decreases with increasing RH from (3.10 ± 0.06) at RH = 10% to

364 (2.41 ± 0.03) at RH = 70% (Fig. 5a). The measured SSA at 120 min is close to unity at 10% and
365 30% RH and decreases with increasing RH (Fig. 5a), indicating negligible NCO formation at low
366 RH but significant NCO formation at RH above 50%. Carboxylates represent the dominant
367 constituent throughout the RH range (i.e., 85% at 10% RH to 47% at 70% RH), while the
368 contributions of oligomers and NCO are small at low RH (2-5% at RH < 40%) and become
369 increasingly significant at high RH (15-23% at RH > 50%) (Fig. 5b). The fraction for PAQ (8%)
370 is nearly invariant with RH. For (NH₄)₂SO₄ particles, the deliquescent and efflorescent points are
371 at 80% and 36% RH, respectively (Li et al., 2021b). At low RH (10% and 30%), aqueous reactions
372 to yield oligomers/NCO are minimal because of small water activity and significantly suppressed
373 protonation and oligomerization. On the other hand, carboxylic acids readily undergo ionic
374 dissociation or acid-base reaction, since organic acids efficiently retain water even at low RH (Xue,
375 2009). The equilibrium vapor pressures for PAQ are much lower than those for organic acids
376 (Table S6), facilitating more efficient condensation. Additionally, wall-loss of COOs is more
377 pronounced at high RH (Li et al., 2021b), explaining the decreased GF with increasing RH.
378 Measurement of gaseous concentrations for COOs shows that wall-loss is 1.5 to 4.6 times more
379 efficient at 70% RH than at 10% RH, while wall loss of *m*-xylene is negligible at both RH levels
380 (Table S7).

381 We determined the total density and the density of the SOA fraction for (NH₄)₂SO₄ seed
382 particles exposed to *m*-xylene oxidation (Fig. 5 c,d). The measured densities are distinct between
383 10 and 70% RH. At 10% RH, the total density decreases monotonically, while the SOA density
384 increases slightly with reaction time, i.e., from 1.27 to 1.39 g cm⁻³ (Fig. 5c), indicating minor
385 oligomers and dominant carboxylic acids at low RH. At 70% RH, the total particle density initially
386 decreases from 1.77 g cm⁻³ to 1.41 g cm⁻³ (at a GF of 1.24) and subsequently increases steadily to

387 1.56 g cm⁻³ at 120 min. The SOA density on (NH₄)₂SO₄ particles increases from 1.26 g cm⁻³ at 10
388 min to 1.55 g cm⁻³ at 120 min (Fig. 5d). The evolution in the densities reflects the variation in the
389 chemical composition. The initial particle growth is dominated by small oligomers, imidazoles
390 from methylglyoxal/methylbutenedial, and early-generation organic acids (e.g., toluic acid), with
391 the densities from 0.98 to 1.27 g cm⁻³ (Table S8). Subsequent particle growth from
392 methylglyoxal/methylbutenedial yields large oligomers, with the densities of 1.71-1.90 g cm⁻³
393 (Table S8).

394 To evaluate the NO_x effects, we performed experiments on (NH₄)₂SO₄ seed particles by
395 varying the initial NO_x concentration from 0 to 500 ppb (Fig. 6). Three major nitrophenols are
396 identified from NO₂ addition to the OH-*m*-xylene adduct, i.e., 4-methyl-2-nitrophenol ($m/z = 154$),
397 dimethyl nitrophenol ($m/z = 168$), and dimethyl-4-nitrocatechol ($m/z = 184$) (Fig. 6a). The
398 production of nitrophenols is much smaller than those for dicarbonyls and organic acids, consistent
399 with a smaller yield (less than 7%) for nitrophenols (Fan and Zhang, 2008). The GF on (NH₄)₂SO₄
400 seed particles with NH₃ decreases from 2.41 ± 0.03 to 2.18 ± 0.03 with 0 to 500 ppb NO_x (Fig. 6b).
401 The SSA decreases significantly from 0.911 ± 0.006 to 0.839 ± 0.003 with increasing NO_x (Fig.
402 6b), because of the formation of light-absorbing nitrophenols (Hems and Abbatt, 2018; Li et al.,
403 2021b). Analysis of particle composition reveals that the decreasing GF with increasing NO_x
404 correlates with simultaneous decreases of carboxylates, oligomers, and NCOs and with increasing
405 nitrophenols in the aerosol-phase (Fig. 6c). Overall, nitrophenols contribute 2% to 4% to the SOA
406 formation. Addition of NO_x not only produces nitrophenols and but also alters the cycling between
407 RO₂ and alkoxy (RO) radicals, leading to re-distributions of COOs. The presence of NO_x decreases
408 dicarbonyls and organic acids, as evident from decreased intensities for oligomers, NCO, and
409 carboxylates in the aerosol-phase with increasing NO_x (Fig. 2h).

410 3.4 COO and SOA Yields

411 From the measured GF and COO concentrations, we derived the γ , which is widely
412 employed to represent aerosol formation in atmospheric models (Zhang et al., 2015). The
413 measured γ varies with the functionality of COOs and RH on $(\text{NH}_4)_2\text{SO}_4$ seed particles (Fig. 7a).
414 Results of the γ values for COOs are also summarized in Table S9. The γ for dicarbonyls is the
415 highest (from 3×10^{-3} to 1.3×10^{-2}) at 70% RH but is significantly reduced (from 3.7×10^{-4} to 1.0
416 $\times 10^{-3}$) at 10% RH, while the γ 's for organic acids, PAQ, and nitrophenols are slightly higher at
417 70% RH. Among the organic acids, the γ correlates with the acid dissociation constant and
418 solubility, which are the highest for pyruvic acid and the lowest for toluic acid. The standard
419 variation in γ (within one σ) among each COO type is within 50%, 40%, 30%, and 15% for
420 dicarbonyls, organic acids, PAQ, and nitrophenols, respectively. From the measured
421 concentrations of COOs and *m*-xylene, we determined the COO yields (Y_{COO}) using eq. 17, by
422 considering four COO species, i.e., dicarbonyls for $i = 1$, carboxylic acids for $i = 2$, PAQ for $i = 3$,
423 and nitrophenols for $i = 4$ (Table S7). The Y_{COO} values for dicarbonyls, organic acids, PAQ, and
424 nitrophenols are 25%, 37%, 5%, and 3%, respectively (Fig. 7b), indicating significant production
425 of COOs from *m*-xylene oxidation.

426 Our work shows significant increase in particle size (Fig. 2a) and constantly varying
427 particle properties, i.e., SSA (Fig. 2b) and density (Fig. 5c,d), which closely correlate with the
428 gaseous COO production (Fig. 1). These results imply a highly nonequilibrium kinetic process
429 leading to SOA formation from *m*-xylene oxidation, which cannot be described by equilibrium
430 partitioning. The gas-to-particle conversion from *m*-xylene oxidation is dominated by several
431 volatile COO species (i.e., organic acids and dicarbonyls) and with minor contribution from
432 condensation of low-volatility COO (i.e., polyhydroxy aromatics/quinones, and nitrophenols) (Fig.

433 5b). In our study, the vapor pressures of the detected gaseous oxidation products for organic acids
434 and dicarbonyls are too large to explain the measured particle growth via equilibrium partitioning
435 (Table S6). Specifically, the saturation vapor pressures of organic acids detected in the particle-
436 phase range from 1.9×10^{-3} to 6.6×10^{-6} atm, while their gas-phase concentrations range from 0.5
437 to 2.5 ppb. Similarly, the saturation vapor pressures of dicarbonyls detected in the particle-phase
438 range from 1.6×10^{-1} to 3.9×10^{-4} atm, while their gas-phase concentrations range from 0.5 to 2.2
439 ppb. The high saturation vapor pressures and low gas-phase concentrations for those COOs render
440 equilibrium partitioning implausible in our experiments. Also, the detection of the particle-phase
441 products confirms that organic acids and dicarbonyls directly participate in heterogeneous
442 reactions to yield low-volatility products. Moreover, volatility-based equilibrium partitioning
443 cannot not explain the variations in the particle size growth, SSA, and chemical compositions on
444 different seed particles (Fig. 3). Clearly, the gas-to-particle conversion from *m*-xylene oxidation
445 involves several distinct heterogeneous processes, including the interfacial interaction, ionic
446 dissociation/acid-base reaction, and nucleophilic oligomerization (Li et al., 2021a,b).

447 We establish a functionality-based SOA formation to predict the aerosol mass
448 concentration (M_{SOA}) from the measured gaseous concentrations and γ 's for COOs using eq. 20.
449 The M_{SOA} is calculated using the averaged γ (Fig. 7a and Table S10) and the measured time-
450 averaged concentrations for each COO type (Table S7). While the production of COOs is
451 dependent on the VOC types and photooxidation, the aerosol-phase reactivity of COOs, as
452 represented by γ , is only dependent on the functionality for a given aerosol type. Thus, SOA
453 formation from various VOC types can be predicted from the production and reactivity for COOs
454 based on the experimental measurements, by categorizing COOs in accordance with their
455 functional groups. In our study, the measured uptake coefficient for each COO type (γ) is derived

456 from the measured particle growth (eqs. 9 and 10), which implicitly accounts for non-continuum
457 diffusion, imperfect accommodation, and evaporation (Zhang et al., 1994; Ravishankara, 1997).

458 To assess the consistency of our approach, we compared the predicted and measured SOA
459 mass yields (Y_{SOA}), according to eq. 21. The predicted Y_{SOA} is $(11 \pm 3)\%$ and $(6 \pm 1)\%$,
460 respectively, at 10% and 70 % RH, comparable to the measured values of $(14 \pm 0.4)\%$ and $(6.3 \pm$
461 $0.2)\%$ on $(\text{NH}_4)_2\text{SO}_4$ seed particles (Fig. 7c). The slight differences between the predicted and
462 measured Y_{SOA} 's are explainable by the uncertainties related to lumping each COO type (i.e.,
463 averaging the γ values) as well as unaccounted low-abundant COO species. To account for the
464 RH-dependent wall loss for COOs, we corrected Y_{SOA} from the measured gaseous concentrations
465 at varying RH (see Methods and Table S7). Such correction results in an increase of about one to
466 four times for Y_{SOA} at 10% and 70% RH, yielding the values of $(20 \pm 4)\%$ and $(32 \pm 7)\%$,
467 respectively (Fig. 7c). Under atmospheric conditions, SOA/BrC formation from *m*-xylene is
468 expected to be enhanced at high RH, because of significantly enhanced aqueous reaction, larger
469 aerosol surface-area, and higher water activity. Field measurements showed significantly enhanced
470 SOA formation with increasing RH during severe haze evolution (Guo et al., 2014; Peng et al.,
471 2021).

472 **4. Conclusions**

473 In this work we have elucidated the production of COOs and their roles in SOA formation
474 from *m*-xylene oxidation. The major advantages of our analytical methodologies lie in
475 simultaneous monitoring of the evolutions of gaseous oxidation products and aerosol properties
476 when seed particles are exposed to the oxidation products, which allows for assessment of multi-
477 generation production of SOA and BrC. Also, our experimental approach remedies the deficiency
478 of wall loss of reactive gaseous and particles, which represents a main obstacle in experimental

479 investigation using environmental chambers (Zhang et al., 2014; Huang et al., 2018). OH-initiated
480 oxidation of *m*-xylene produces four distinct COO types consisting of dicarbonyls, carboxylic
481 acids, polyhydroxy aromatics/quinones, and nitrophenols from early-generation (P₂ and P₃), with
482 the yields of 25%, 37%, 5%, and 3%, respectively. SOA formation occurs via several
483 heterogeneous processes, including interfacial interaction, ionic dissociation/acid-base reaction,
484 and oligomerization, with the yields of (20 ± 4)% at 10% RH and (32 ± 7)% at 70% RH. The
485 identified aerosol-phase products include dominant oligomers, N-heterocycles/N-heterochains,
486 and carboxylates at high RH and dominant carboxylates at low RH, along with small amounts of
487 PAQ and nitrophenols (in the presence of NO_x). The nitrogen-containing organics consisting of
488 N-heterocycles, N-heterochains, and nitrophenols are light-absorbing, characterized by low SSA.
489 The measured γ for COOs is dependent on the functionality, ranging from 3.7×10^{-4} to 1.3×10^{-2} .
490 A kinetic framework is developed to predict SOA formation from the concentration and γ for
491 COOs. Our results illustrate that SOA formation from *m*-xylene oxidation is accurately quantified
492 from the abundance and reactivity for COOs (i.e., eq. 20). Notably, this kinetic framework
493 accounts for the interfacial process (i.e., mass accommodation) as well as aqueous reactions (i.e.,
494 oligomerization and acid-base reactions) without the assumption of gas-particle equilibrium. We
495 envisage that this functionality-based approach is applicable to predict SOA formation from VOC
496 photooxidation using experiment/field measured or model-simulated COOs, aerosol surface area,
497 and reactivity. We conclude that photochemical oxidation of *m*-xylene represents a major source
498 for SOA and BrC formation under urban conditions, because of its large abundance, high reactivity
499 with OH, and high yields for COOs.

500 **ACKNOWLEDGEMENTS**

501 This research was supported by the Robert A. Welch Foundation (Grant A-1417). Y.L. was
502 supported by a dissertation Fellowship at Texas A&M University.

503 REFERENCES

- 504 Atkinson, R. Atmospheric Chemistry of VOCs and NO_x. *Atmos. Environ.*, 34, 2063–2101, 2000.
- 505 Calvert, J. G., Atkinson, R., Becker, K. H., Kamens, R. M., Seinfeld, J. H., Wallington, T. H., and
506 Yarwood, G.: The Mechanisms of Atmospheric Oxidation of Aromatic Hydrocarbons, Oxford
507 University Press: New York., 2002.
- 508 Claflin, M. S. and Ziemann, P. J.: Thermal desorption behavior of hemiacetal, acetal, ether, and
509 ester oligomers, *Aerosol Sci. Technol.*, 53(4), 473–484, doi:10.1080/02786826.2019.1576853,
510 2019.
- 511 Dotan, I., Albritton, D. L., Lindinger, W. and Pahl, M.: Mobilities of CO₂⁺, N₂H⁺, H₃O⁺,
512 H₃O⁺·H₂O, and H₃O⁺·(H₂O)₂ ions in N₂, *J. Chem. Phys.*, 65(11), 5028–5030,
513 doi:10.1063/1.432943, 1976.
- 514 Fan, J., and Zhang, R.: Density Functional Theory Study on OH-Initiated Atmospheric Oxidation
515 of m-Xylene, *J. Phys. Chem. A*, 112(18), 4314–4323, doi:10.1021/jp077648j, 2008.
- 516 Faust, J. A., Wong, J. P. S., Lee, A. K. Y., and Abbatt, J. P. D.: Role of Aerosol Liquid Water in
517 Secondary Organic Aerosol Formation from Volatile Organic Compounds, *Environ. Sci. Technol.*,
518 51, 1405– 1413, 2017.
- 519 Finlayson-Pitts, B. J., and Pitts, J. N.: *Chemistry of the Upper and Lower Atmosphere: Theory,*
520 *Experiments and Applications*, Academic Press, San Diego, 2000.
- 521 Fortner, E. C., Zheng, J., Zhang, R., Berk Knighton, W., Volkamer, R. M., Sheehy, P., Molina, L.,
522 and André, M.: Measurements of Volatile Organic Compounds Using Proton Transfer Reaction –
523 Mass Spectrometry during the MILAGRO 2006 Campaign, *Atmos. Chem. Phys.*, 9(2), 467–481,
524 doi:10.5194/acp-9-467-2009, 2009.
- 525 Fortner, E.C., Zhao, J., and Zhang, R.: Development of ion drift-chemical ionization mass
526 spectrometry, *Anal. Chem.*, 76, 5436-5440, 2004.
- 527 Fountoukis, C. and Nenes, A.: SORROPIA II: A Computationally Efficient Thermodynamic
528 Equilibrium Model for K⁺–Ca²⁺–Mg²⁺–NH₄⁺–Na⁺–SO₄²⁻–NO₃⁻–Cl–H₂O Aerosols., *Atmos.*
529 *Chem. Phys.*, 7(17), 4639–4659, doi:10.5194/acp-7-4639-2007, 2007.
- 530 Garmash, O., Rissanen, M. P., Pullinen, I., Schmitt, S., Kausiala, O., Tillmann, R., Zhao, D.,
531 Percival, C., Bannan, T. J., Priestley, M., Hallquist, Å. M., Kleist, E., Kiendler-Scharr, A.,
532 Hallquist, M., Berndt, T., McFiggans, G., Wildt, J., Mentel, T. F., and Ehn, M.: Multi-generation
533 OH oxidation as a source for highly oxygenated organic molecules from aromatics, *Atmos. Chem.*
534 *Phys.*, 20(1), 515–537, doi:10.5194/acp-20-515-2020, 2020.

535 Guo, S., Hu, M., Zamora, M. L., Peng, J., Shang, D., Zheng, J., Du, Z., Wu, Z., Shao, M., Zeng,
536 L., Molina, M. J., and Zhang, R.: Elucidating severe urban haze formation in China, *Proc. Natl.*
537 *Acad. Sci. USA*, 111(49), 17373–17378, doi:10.1073/pnas.1419604111, 2014.

538 Guo, S., Hu, M., Lin, Y., Gomez-Hernandez, M., Zamora, M. L., Peng, J., Collins, D. R., and
539 Zhang, R.: OH-Initiated Oxidation of m-Xylene on Black Carbon Aging, *Environ. Sci. Technol.*,
540 50(16), 8605–8612, doi:10.1021/acs.est.6b01272, 2016.

541 Guo, S., Hu, M., Peng, J., Wu, Z., Zamora, M. L., Shang, D., Du, Z., Zheng, J., Fang, X., Tang,
542 R., Wu, Y., Zeng, L., Shuai, S., Zhang, W., Wang, Y., Ji, Y., Li, Y., Zhang, A. L., Wang, W.,
543 Zhang, F., Zhao, J., Gong, X., Wang, C., Molina, M. J. and Zhang, R.: Remarkable nucleation
544 and growth of ultrafine particles from vehicular exhaust, *Proc. Natl. Acad. Sci.*, 117(7), 3427–
545 3432, doi:10.1073/pnas.1916366117, 2020.

546 De Haan, D. O., Hawkins, L. N., Kononenko, J. A., Turley, J. J., Corrigan, A. L., and Tolbert, M.
547 A., Jimenez, J. L.: Formation of Nitrogen- Containing Oligomers by Methylglyoxal and Amines
548 in Simulated Evaporating Cloud Droplets, *Environ. Sci. Technol.*, 45, 984– 991, 2011.

549 De Haan, D. O., Hawkins, L. N., Welsh, H. G., Pednekar, R., Casar, J. R., Pennington, E. A., de
550 Loera, A., Jimenez, N. G., Symons, M. A., Zauscher, M., Pajunoja, A., Caponi, L., Cazaunau, M.,
551 Formenti, P., Gratien, A., Pangui, E., and Doussin, J.-F.: Brown Carbon Production in
552 Ammonium- or Amine-Containing Aerosol Particles by Reactive Uptake of Methylglyoxal and
553 Photolytic Cloud Cycling, *Environ. Sci. Technol.*, 51(13), 7458–7466,
554 doi:10.1021/acs.est.7b00159, 2017.

555 Heald, C. L., Jacob, D. J., Park, R. J., Russell, L. M., Huebert, B. J., Seinfeld, J. H., Liao, H., and
556 Weber, R. J.: A Large Organic Aerosol Source in the Free Troposphere Missing from Current
557 Models. *Geophys. Res. Lett.*, 32, 1–4, 2005.

558 Hems, R. F., and Abbatt, J. P. D.: Aqueous Phase Photo-oxidation of Brown Carbon Nitrophenols:
559 Reaction Kinetics, Mechanism, and Evolution of Light Absorption, *ACS Earth Sp. Chem.*, 2(3),
560 225–234, doi:10.1021/acsearthspacechem.7b00123, 2018.

561 Hodzic, A., Kasibhatla, P. S., Jo, D. S., Cappa, C. D., Jimenez, J. L., Madronich, S., and Park, R.
562 J.: Rethinking the Global Secondary Organic Aerosol (SOA) Budget: Stronger Production, Faster
563 Removal, Shorter Lifetime. *Atmos. Chem. Phys.*, 16, 7917–7941, 2016.

564 Hua, W., Jubb, A. M., and Allen, H. C.: Electric Field Reversal of Na₂SO₄, (NH₄)₂SO₄, and
565 Na₂CO₃ Relative to CaCl₂ and NaCl at the Air/Aqueous Interface Revealed by Heterodyne
566 Detected Phase-Sensitive Sum Frequency, *J. Phys. Chem. Lett.*, 2(20), 2515–2520,
567 doi:10.1021/jz200888t, 2011.

568 Huang, Y., Zhao, R., Charan, S. M., Kenseth, C. M., Zhang, X., and Seinfeld, J. H.: Unified Theory
569 of Vapor–Wall Mass Transport in Teflon-Walled Environmental Chambers, *Environ. Sci.*
570 *Technol.*, 52(4), 2134–2142, doi:10.1021/acs.est.7b05575, 2018.

571 Intergovernmental Panel on Climate Change (IPCC). *Climate Change 2013: The Physical Science*
572 *Basis. Contribution of Working Group I to the Fifth Assessment Report of the Intergovernmental*
573 *Panel on Climate Change*. Cambridge University Press, 2013.

574 Jenkin, M. E., Saunders, S. M., Wagner, V., and Pilling, M. J.: Protocol for the development of
575 the Master Chemical Mechanism, MCM v3 (Part B): tropospheric degradation of aromatic volatile
576 organic compounds, *Atmos. Chem. Phys.*, 3(1), 181–193, doi:10.5194/acp-3-181-2003, 2003.

577 Ji, Y., Zhao, J., Terazono, H., Misawa, K., Levitt, N. P., Li, Y., Lin, Y., Peng, J., Wang, Y., Duan,
578 L., Pan, B., Zhang, F., Feng, X., An, T., Marrero-Ortiz, W., Secrest, J., Zhang, A. L., Shibuya, K.,
579 Molina, M. J., and Zhang, R.: Reassessing the atmospheric oxidation mechanism of toluene, *Proc.*
580 *Natl. Acad. Sci. USA*, 114(31), 8169–8174, doi:10.1073/pnas.1705463114, 2017.

581 Ji, Y., Shi, Q., Li, Y., An, T., Zheng, J., Peng, J., Gao, Y., Chen, J., Li, G., Wang, Y., Zhang, F.,
582 Zhang, A. L., Zhao, J., Molina, M. J., and Zhang, R.: Carbenium ion-mediated oligomerization of
583 methylglyoxal for secondary organic aerosol formation, *Proc. Natl. Acad. Sci. USA*, 117(24),
584 13294 LP – 13299, doi:10.1073/pnas.1912235117, 2020.

585 Jia, L., and Xu, Y.: Effects of Relative Humidity on Ozone and Secondary Organic Aerosol
586 Formation from the Photooxidation of Benzene and Ethylbenzene, *Aerosol Sci. Technol.*, 48(1),
587 1–12, doi:10.1080/02786826.2013.847269, 2014.

588 Jia, L., and Xu, Y.: Different roles of water in secondary organic aerosol formation from toluene
589 and isoprene, *Atmos. Chem. Phys.*, 18(11), 8137–8154, doi:10.5194/acp-18-8137-2018, 2018.

590 Li, G., Zhang, R., Fan, J., and Tie, X.: Impacts of biogenic emissions on photochemical ozone
591 production in Houston, Texas, *J. Geophys. Res.*, 112, D10309, doi:10.1029/2006JD007924, 2007.

592 Li, Y., Ji, Y., Zhao, J., Wang, Y., Shi, Q., Peng, J., Wang, Y., Wang, C., Zhang, F., Wang, Y.,
593 Seinfeld, J. H., and Zhang, R.: Unexpected Oligomerization of Small α -Dicarbonyls for Secondary
594 Organic Aerosol and Brown Carbon Formation, *Environ. Sci. Technol.*, 55(8), 4430–4439,
595 doi:10.1021/acs.est.0c08066, 2021a.

596 Li, Y., Zhao, J., Wang, Y., Seinfeld, J. H., and Zhang, R.: Multigeneration Production of Secondary
597 Organic Aerosol from Toluene Photooxidation, *Environ. Sci. Technol.*, 55, 8592–8603,
598 doi:10.1021/acs.est.1c02026, 2021b.

599 Liu, J., Zhang, F., Xu, W., Sun, Y., Chen, L., Li, S., Ren, J., Hu, B., Wu, H., and Zhang, R.:
600 Hygroscopicity of Organic Aerosols Linked to Formation Mechanisms, *Geophys. Res. Lett.*, 48(4),
601 e2020GL091683, doi:https://doi.org/10.1029/2020GL091683, 2021.

602 Marrero-Ortiz, W., Hu, M., Du, Z., Ji, Y., Wang, Y. Y., Guo, S., Lin, Y., Gomez-Hernandez, M.,
603 Peng, J., Li, Y., Secrest, J., Zamora, M. L., Wang, Y. Y., An, T., and Zhang, R.: Formation and
604 Optical Properties of Brown Carbon from Small α -Dicarbonyls and Amines, , 53(1), 117–126,
605 doi:10.1021/acs.est.8b03995, 2019.

606 McMurry, P. H. and Rader, D. J.: Aerosol Wall Losses in Electrically Charged Chambers, *Aerosol*
607 *Sci. Technol.*, 4(3), 249–268, doi:10.1080/02786828508959054, 1985.

608 Molina, L. T.: Introductory lecture: air quality in megacities, *Faraday Discuss*, 226, 9-52,
609 10.1039/d0fd00123f, 2021.

610 Moise, T., Flores, J. M., and Rudich, Y.: Optical Properties of Secondary Organic Aerosols and
611 Their Changes by Chemical Processes, *Chem. Rev.*, 115, 4400–4439, 2015.

612 Molteni, U., Bianchi, F., Klein, F., El Haddad, I., Frege, C., Rossi, M. J., Dommen, J., and
613 Baltensperger, U.: Formation of highly oxygenated organic molecules from aromatic compounds,
614 *Atmos. Chem. Phys.*, 18(3), 1909–1921, doi:10.5194/acp-18-1909-2018, 2018.

615 National Academies of Sciences Engineering and Medicine (NASEM): The Future of Atmospheric
616 Chemistry Research: Remembering Yesterday, Understanding Today, Anticipating Tomorrow,
617 The National Academies Press, Washington, DC., 2016.

618 Ng, N. L., Kroll, J. H., Chan, A. W. H., Chhabra, P. S., Flagan, R. C., and Seinfeld, J. H.: Secondary
619 organic aerosol formation from m-xylene, toluene, and benzene, *Atmos. Chem. Phys.*, 7(14),
620 3909–3922, doi:10.5194/acp-7-3909-2007, 2007.

621 Nishino, N., Arey, J., and Atkinson, R.: Formation Yields of Glyoxal and Methylglyoxal from the
622 Gas-Phase OH Radical-Initiated Reactions of Toluene, Xylenes, and Trimethylbenzenes as a
623 Function of NO₂ Concentration, *J. Phys. Chem. A*, 114(37), 10140–10147,
624 doi:10.1021/jp105112h, 2010.

625 Peng, J., Hu, M., Shang, D., Wu, Z., Du, Z., Tan, T., Wang, Y., Zhang, F., and Zhang, R.:
626 Explosive secondary aerosol formation during severe haze in the North China Plain, *Environ. Sci.*
627 *Technol.*, 55(4), 2189–2207, 2021.

628 Pope, C. A., III, Burnett, R. T., Thun, M. J., Calle, E. E., Krewski, D., Ito, K., and Thurston, G.
629 D.: Lung Cancer, Cardiopulmonary Mortality, and Long-Term Exposure to Fine Particulate Air
630 Pollution. *J. Am. Med. Assoc.*, 287, 1132–1141, 2002.

631 Qi, X., Zhu, S., Zhu, C., Hu, J., Lou, S., Xu, L., Dong, J. and Cheng, P.: Smog chamber study of
632 the effects of NO_x and NH₃ on the formation of secondary organic aerosols and optical properties
633 from photo-oxidation of toluene, *Sci. Total Environ.*, 727, 138632,
634 doi:https://doi.org/10.1016/j.scitotenv.2020.138632, 2020.

635 Ravishankara, A.R.: Heterogeneous and multiphase chemistry in the troposphere, *Science* 276,
636 1058-1065, 1997.

637 Schwantes, R. H., Schilling, K. A., McVay, R. C., Lignell, H., Coggon, M. M., Zhang, X.,
638 Wennberg, P. O., and Seinfeld, J. H.: Formation of highly oxygenated low-volatility products from
639 cresol oxidation, *Atmos. Chem. Phys.*, 17(5), 3453–3474, doi:10.5194/acp-17-3453-2017, 2017.

640 Seinfeld, J. H., and Pandis, S. N.: Atmospheric chemistry and physics: from air pollution to climate
641 change, John Wiley & Sons., 2016.

642 Shi, Q., Zhang, W., Ji, Y., Wang, J., Qin, D., Chen, J., Gao, Y., Li, G., and An, T.: Enhanced
643 uptake of glyoxal at the acidic nanoparticle interface: implications for secondary organic aerosol
644 formation, *Environ. Sci. Nano*, 7, 1126–1135, 2020.

645 Shrivastava, M., Cappa, C. D., Fan, J., Goldstein, A. H., Guenther, A. B., Jimenez, J. L., Kuang,
646 C., Laskin, A., Martin, S. T., Ng, N. L., Petaja, T., Pierce, J. R., Rasch, P. J., Roldin, P., Seinfeld,
647 J. H., Shilling, J., Smith, J. N., Thornton, J. A., Volkamer, R., Wang, J., Worsnop, D. R., Zaveri,
648 R. A., Zelenyuk, A., and Zhang, Q.: Recent advances in understanding secondary organic aerosol:
649 Implications for global climate forcing, *Rev. Geophys.*, 55(2), 509–559,
650 doi:10.1002/2016RG000540, 2017.

651 Song, C., Na, K., Warren, B., Malloy, Q., and Cocker, D. R.: Secondary Organic Aerosol
652 Formation from m-Xylene in the Absence of NO_x, *Environ. Sci. Technol.*, 41(21), 7409–7416,
653 doi:10.1021/es070429r, 2007.

654 Suh, I., Lei, W., and Zhang, R.: Experimental and theoretical studies of isoprene reaction with
655 NO₃, *J. Phys. Chem.*, 105, 6471–6478, 2001.

656 Tan, Y., Lim, Y. B., Altieri, K. E., Seitzinger, S. P., and Turpin, B. J.: Mechanisms leading to
657 oligomers and SOA through aqueous photooxidation: insights from OH radical oxidation of acetic
658 acid and methylglyoxal, *Atmos. Chem. Phys.*, 11, 18319–18347, 2012.

659 Wang, G., Zhang, F., Peng, J., Duan, L., Ji, Y., Marrero-Ortiz, W., Wang, J., Li, J., Wu, C., Cao,
660 C., Wang, Y., Zheng, J., Secrest, J., Li, Y., Wang, Y., Li, H., Li, N., and Zhang, R.: Particle acidity
661 and sulfate production during severe haze events in China cannot be reliably inferred by assuming
662 a mixture of inorganic salts, *Atmos. Chem. Phys.*, 18, 10123–10132, doi: 10.5194/acp-18-10123-
663 2018, 2018.

664 Wang, L., Khalizov, A. F., Zheng, J., Xu, W., Ma, Y., Lal, V. and Zhang, R.: Atmospheric
665 nanoparticles formed from heterogeneous reactions of organics, *Nat. Geosci.*, 3(4), 238–242,
666 doi:10.1038/ngeo778, 2010.

667 Wang, M., Chen, D., Xiao, M., Ye, Q., Stolzenburg, D., Hofbauer, V., Ye, P., Vogel, A. L.,
668 Mauldin, R. L., Amorim, A., Baccarini, A., Baumgartner, B., Brilke, S., Dada, L., Dias, A.,
669 Duplissy, J., Finkenzeller, H., Garmash, O., He, X.-C., Hoyle, C. R., Kim, C., Kvashnin, A.,
670 Lehtipalo, K., Fischer, L., Molteni, U., Petäjä, T., Pospisilova, V., Quéléver, L. L. J., Rissanen, M.,
671 Simon, M., Tauber, C., Tomé, A., Wagner, A. C., Weitz, L., Volkamer, R., Winkler, P. M., Kirkby,
672 J., Worsnop, D. R., Kulmala, M., Baltensperger, U., Dommen, J., El-Haddad, I., and Donahue, N.
673 M.: Photo-oxidation of Aromatic Hydrocarbons Produces Low-Volatility Organic Compounds,
674 *Environ. Sci. Technol.*, 54(13), 7911–7921, doi:10.1021/acs.est.0c02100, 2020.

675 Wang, Y., Khalizov, A., Levy, M., and Zhang, R.: Light absorbing aerosols and their atmospheric
676 impacts, *Atmos. Environ.*, 81, 713–715, doi:10.1016/j.atmosenv.2013.09.034, 2013.

677 Wang, Y., Lee, K.-H., Lin, Y., Levy, M., and Zhang, R.: Distinct effects of anthropogenic aerosols
678 on tropical cyclones, *Nature Clim. Change*, 4, 368–373, doi:10.1038/nclimate2144 2014.

679 Wennberg, P. O., Bates, K. H., Crouse, J. D., Dodson, L. G., McVay, R. C., Mertens, L. A.,
680 Nguyen, T. B., Praske, E., Schwantes, R. H., Smarte, M. D., St Clair, J. M., Teng, A. P., Zhang,
681 X., and Seinfeld, J. H.: Gas-Phase Reactions of Isoprene and Its Major Oxidation Products, *Chem.*
682 *Rev.*, 118, 3337–3390, 2018.

683 Xue, H., Khalizov, A. F., Wang, L., Zheng, J., and Zhang, R.: Effects of Coating of Dicarboxylic
684 Acids on the Mass–Mobility Relationship of Soot Particles, *Environ. Sci. Technol.*, 43(8), 2787–
685 2792, doi:10.1021/es803287v, 2009.

686 Yuan, B., Koss, A. R., Warneke, C., Coggon, M., Sekimoto, K. and de Gouw, J. A.: Proton-
687 Transfer-Reaction Mass Spectrometry: Applications in Atmospheric Sciences, *Chem. Rev.*,
688 117(21), 13187–13229, doi:10.1021/acs.chemrev.7b00325, 2017.

689 Zhang, D., Lei, W., and Zhang, R.: Mechanism of OH formation from ozonolysis of isoprene:
690 Kinetics and product yields, *Chem. Phys. Lett.* 358, 171-179, 2002.

691 Zhang, F., Wang, Y., Peng, J., Chen, L., Sun, Y., Duan, L., Ge, X., Li, Y., Zhao, J., Liu, C., Zhang,
692 X., Zhang, G., Pan, Y., Wang, Y., Zhang, A.L., Ji, Y., Wang, G., Hu, M., Molina, M.J., and Zhang,
693 R.: An unexpected catalyst dominates formation and radiative forcing of regional haze, *Proc. Natl.*
694 *Acad. Sci. USA*, 117, 3960-3966, doi/10.1073/pnas.1919343117, 2020.

695 Zhang, Q., Xu, Y., and Jia, L.: Secondary organic aerosol formation from OH-initiated oxidation
696 of m-xylene: effects of relative humidity on yield and chemical composition, *Atmos. Chem. Phys.*,
697 19(23), 15007–15021, doi:10.5194/acp-19-15007-2019, 2019.

698 Zhang, R., Leu, M.T., and Keyser, L.F.: Heterogeneous reactions involving ClONO₂, HCl, and
699 HOCl on liquid sulfuric acid surfaces, *J. Phys. Chem.*, 98, 13563-13574, 1994.

700 Zhang, R., Suh, I., Zhao, J., Zhang, D., Fortner, E. C., Tie, X., Molina, L. T. and Molina, M. J.:
701 Atmospheric New Particle Formation Enhanced by Organic Acids, *Science* (80-.), 304(5676),
702 1487 LP – 1490, doi:10.1126/science.1095139, 2004.

703 Zhang, R., Wang, L., Khalizov, A. F., Zhao, J., Zheng, J., McGraw, R. L., and Molina, L. T.:
704 Formation of nanoparticles of blue haze enhanced by anthropogenic pollution, *Proc. Natl. Acad.*
705 *Sci. USA*, 106, doi:10.1073/pnas.0910125106, 17650-17654, 2009.

706 Zhang, R., Wang, G., Guo, S., Zamora, M. L., Ying, Q., Lin, Y., Wang, W., Hu, M., and Wang,
707 Y.: Formation of Urban Fine Particulate Matter, *Chem. Rev.*, 115(10), 3803–3855,
708 doi:10.1021/acs.chemrev.5b00067, 2015.

709 Zhang, R., Johnson, N.M., and Li Y.: Establishing the exposure-outcome relation between airborne
710 particulate matter and children’s health, *Thorax*, 76, doi.org/10.1136/thoraxjnl-2021-217017, 2021.

711 Zhang, X., Cappa, C. D., Jathar, S. H., McVay, R. C., Ensberg, J. J., Kleeman, M. J., and Seinfeld,
712 J. H.: Influence of Vapor Wall Loss in Laboratory Chambers on Yields of Secondary Organic
713 Aerosol. *Proc. Natl. Acad. Sci. U.S.A.*, 111, 5802–5807, 2014.

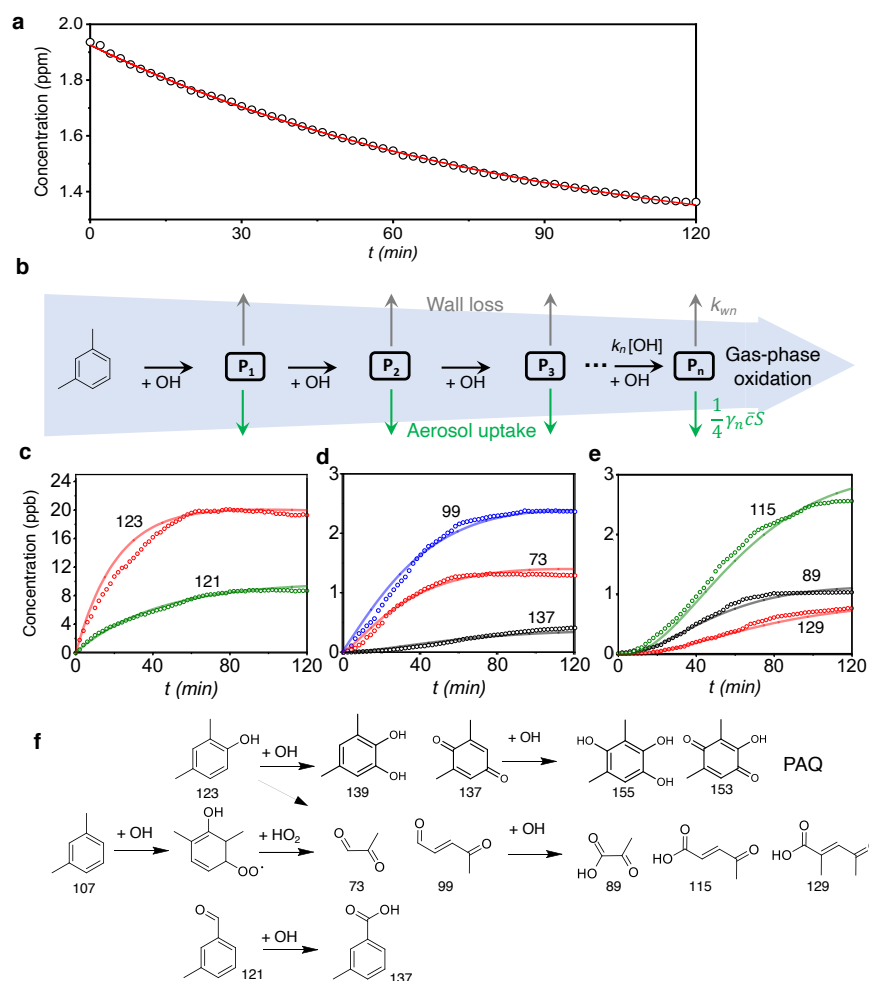
714 Zhao, J., and Zhang, R.: Proton transfer reaction rate constants between hydronium ion (H₃O⁺) and
715 volatile organic compounds, *Atmos. Environ.*, 38(14), 2177–2185,
716 doi:https://doi.org/10.1016/j.atmosenv.2004.01.019, 2004.

717 Zhao, J., Zhang, R., Fortner, E.C., and North, S.W.: Quantification of hydroxycarbonyls from OH-
718 isoprene reactions, *J. Am. Chem. Soc.*, 126, 2686-2687, 2004.

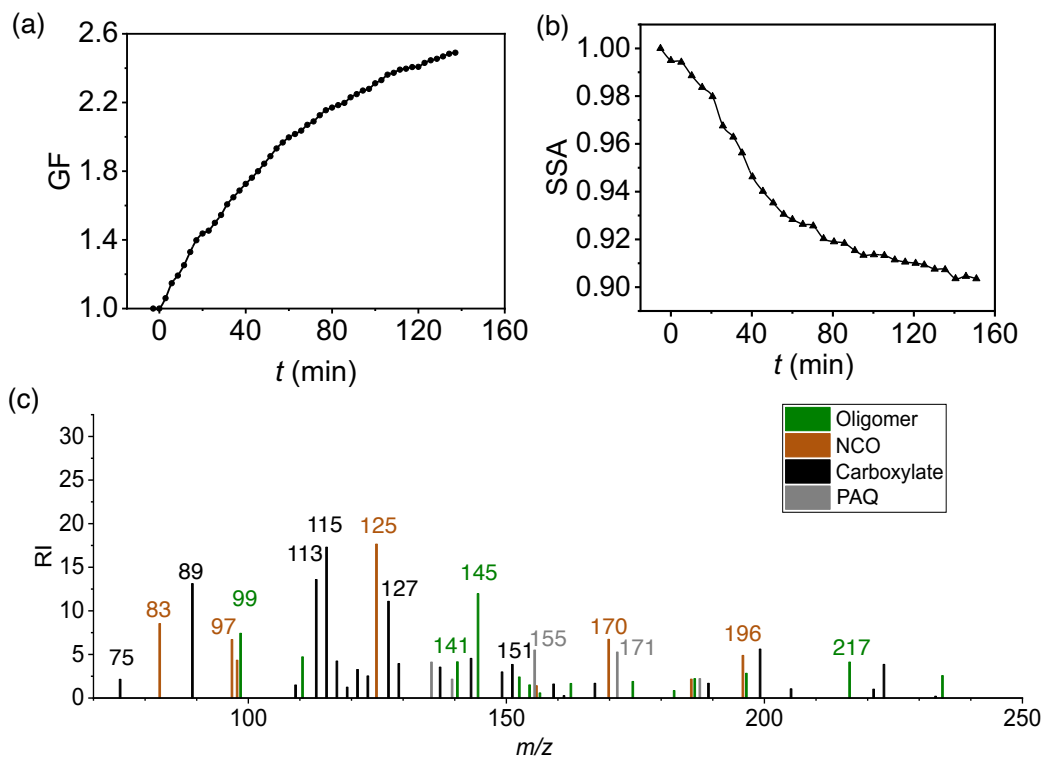
719 Zhao, J., Zhang, R., Misawa, K., and Shibuya, K.: Experimental product study of the OH-initiated
720 oxidation of m-xylene, *J. Photochem. Photobiol. A Chem.*, 176(1), 199–207,
721 doi:<https://doi.org/10.1016/j.jphotochem.2005.07.013>, 2005.

722 Zhu, J., Penner, J. E., Lin, G., Zhou, C., Xu, L., and Zhuang, B.: Mechanism of SOA formation
723 determines magnitude of radiative effects, *P. Natl. Acad. Sci. USA*, 114, 12685–12690,
724 <https://doi.org/10.1073/pnas.1712273114>, 2017.

725



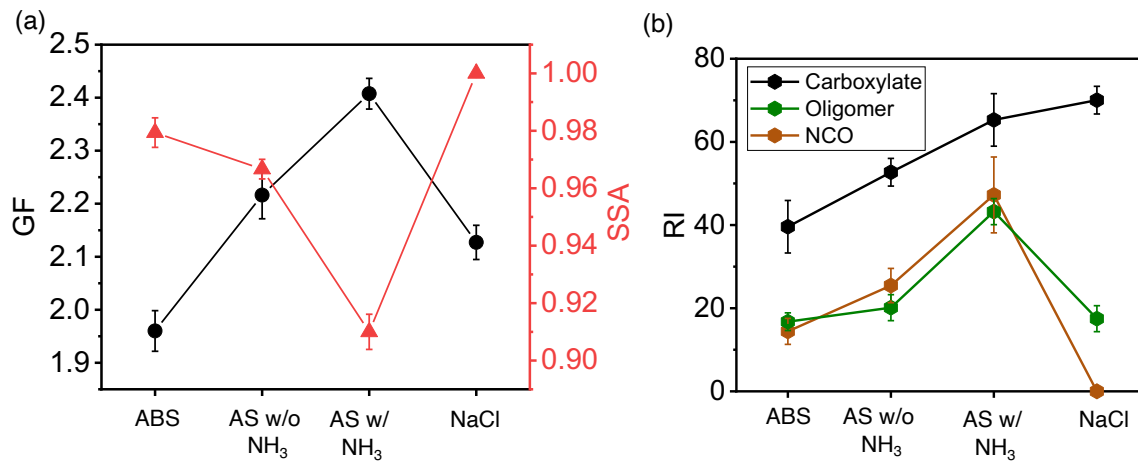
727
 728 **Figure 1.** OH-initiated photooxidation of *m*-
 729 xylene. (a) Time-dependent concentration of *m*-
 730 xylene. The symbols are from the measurements, and the red solid line corresponds to exponential
 731 fitting of the *m*-xylene concentration. The initial concentration for *m*-xylene and the estimated
 732 steady-state concentration for OH are 1940 ppb and 2.1×10^6 molecules cm^{-3} , respectively, with a
 733 bimolecular rate constant of 2.4×10^{-11} cm^3 molecule $^{-1}$ s $^{-1}$. (b) Schematic representation leading to
 734 the multi-generation product, P_n , where n denotes the sequence of OH-initiated oxidation. The
 735 black, gray, and green arrows denote the gas-phase oxidation, chamber wall loss, and aerosol
 736 uptake, respectively. k_n and k_{wn} are the rate coefficients for the gas-phase oxidation and wall loss,
 737 respectively, γ_n represents the aerosol uptake coefficient, \bar{c} is the thermal velocity, and S is the
 738 aerosol surface area. (c-e) Time-dependent gas-phase concentrations of P_1 (c), P_2 (d), and P_3 (e)
 739 products. The symbols are from measurements, and the solid curves are simulated according to the
 740 tri-exponential kinetics. (f) The gaseous oxidation pathways leading to the detected products. The
 741 top row corresponds to the pathways leading to polyhydroxy aromatics/quinones (PAQ). The
 742 numbers in (c) to (f) represents the mass to charge ratio (m/z). All experiments are carried out for
 743 $(\text{NH}_4)_2\text{SO}_4$ seed particles with 19 ppb NH_3 at 298 K and $\text{RH} = 70\%$. Initiation of photooxidation
 by ultraviolet light occurs at $t = 0$.



744

745 **Figure 2.** SOA and BrC formation from *m*-xylene photooxidation. Time-dependent growth factor
 746 ($GF = D_p/D_0$, a) and single scattering albedo (SSA, b) of seed particles exposed to *m*-xylene
 747 oxidation products. (c) Chemical speciation of aerosol-phase products by TD-ID-CIMS. Initiation
 748 of photooxidation by ultraviolet light occurred at $t = 0$. RI denotes the relative intensity for the
 749 integrated peak area during thermal desorption. All experiments are carried out for $(NH_4)_2SO_4$ seed
 750 particles with 19 ppb NH_3 at 298 K and $RH = 70\%$.

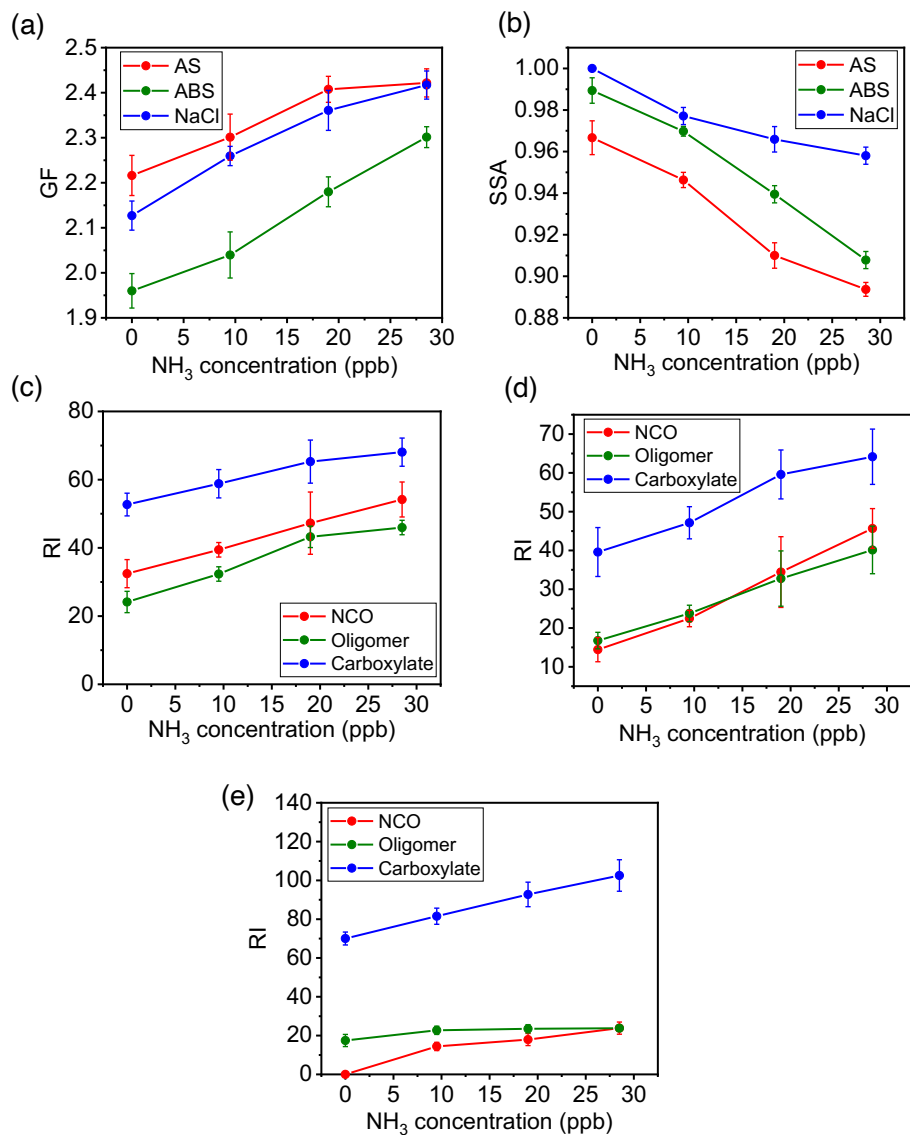
751



752

753 **Figure 3.** Dependence of SOA/BrC formation on seed particles. (a) GF (black) and SSA (red) at
 754 120 mins of exposure for $(\text{NH}_4)_2\text{SO}_4$ particles in the presence (AS w/ NH_3) and absence (AS w/o
 755 NH_3) of 19 ppb NH_3 and for NH_4HSO_4 (ABS) and NaCl particles in the absence of NH_3 . (b)
 756 Aerosol-phase relative intensity (RI) for carboxylates (black), oligomers (green), and NCO (brown)
 757 on different seed particles. The error bar denotes 1σ of 3 replicated measurements. All particle
 758 properties were measured relevant to dry conditions (less than 5% RH) and were dominantly
 759 contributed by non-volatile aerosol-phase products.

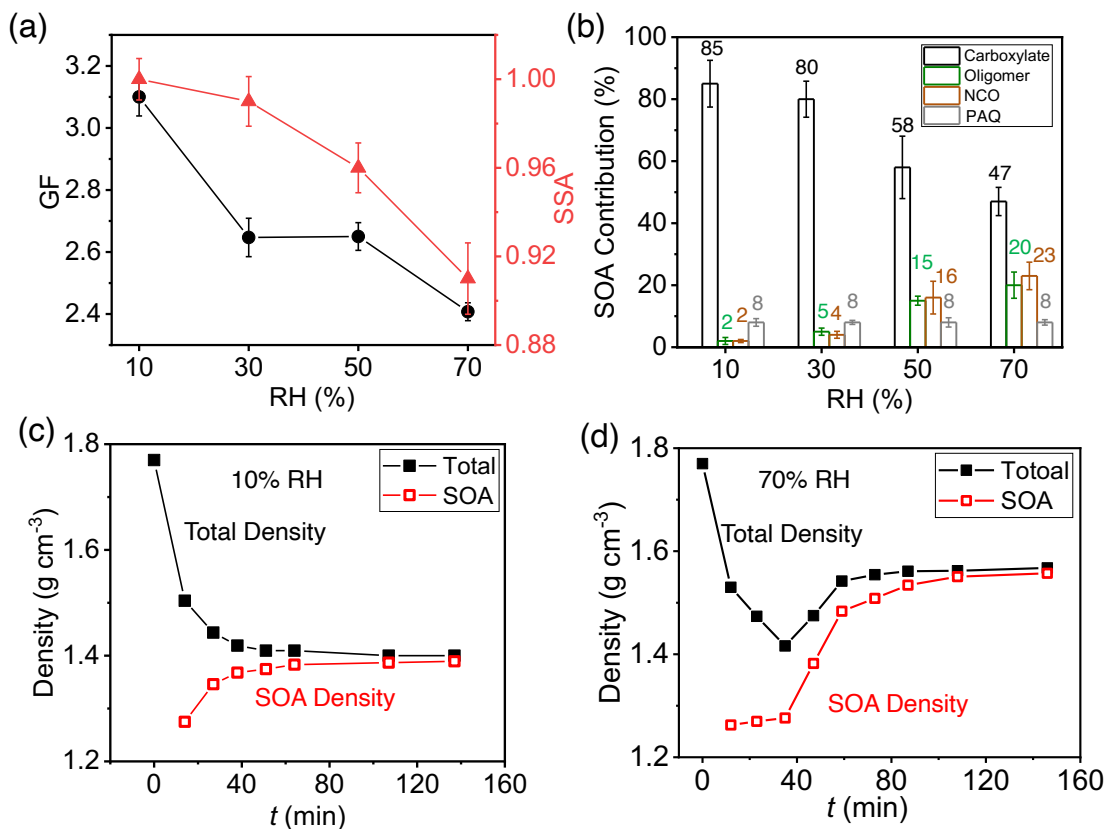
760



761

762 **Figure 4.** Variation of SOA formation with seed particles and NH₃ concentration. (a,b) growth
 763 factor (a) and SSA (b) at $t = 120$ min with varying NH₃ concentration between 0 and 27 ppb for
 764 ammonium sulfate (AS, red), ammonium bisulfate (ABS, green), and sodium chloride (NaCl,
 765 blue) seed particles. (c-e) Aerosol-phase mass relative intensity (RI) for NCO (red), oligomers
 766 (green), and carboxylates (blue) on AS (c), ABS (d), and NaCl (e) seed particles. The error bar
 767 denotes 1σ of 3 replicated measurements.

768

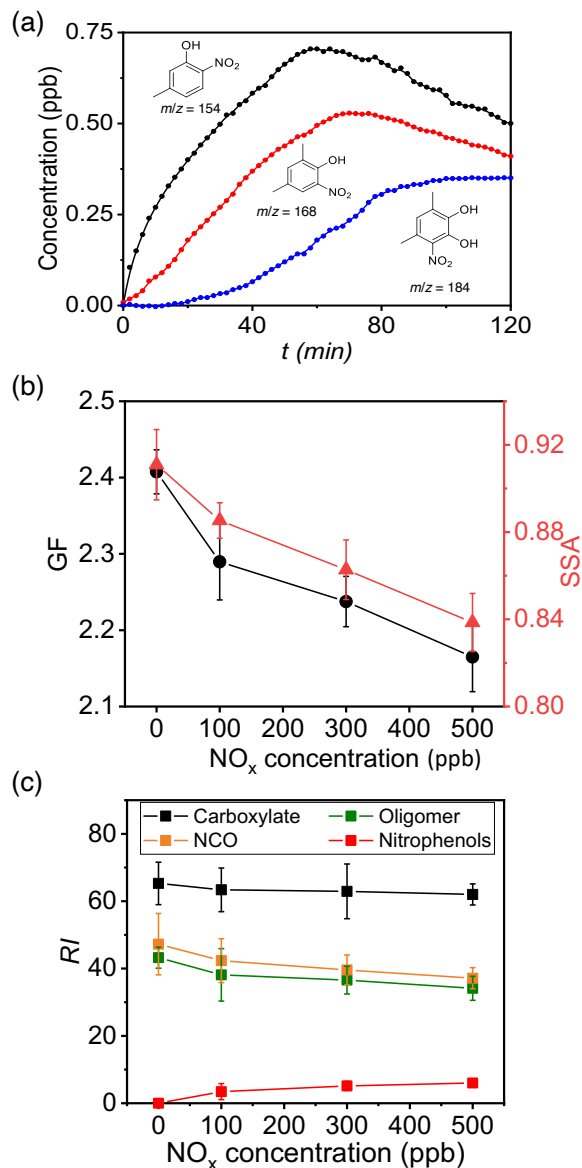


769

770 **Figure 5.** Dependence of SOA/BrC formation on RH. (a) GF (black) and SSA (red) at 120 min
 771 with varying RH from 10% to 70%. (b) Contribution of COOs to SOA formation with varying RH
 772 from 10% to 70%: carboxylate (black), oligomers (green), NCO (brown), and PAQ (gray) to SOA
 773 formation. The number denotes the percentage contribution (%) of each type of aerosol-phase
 774 products. (c,d) Time-dependent particle (black) and SOA (red) densities of seed particles exposed
 775 to *m*-xylene oxidation products at RH = 10% (c) and 70% (d), respectively. The error bar denotes
 776 1σ of 3 replicated measurements.

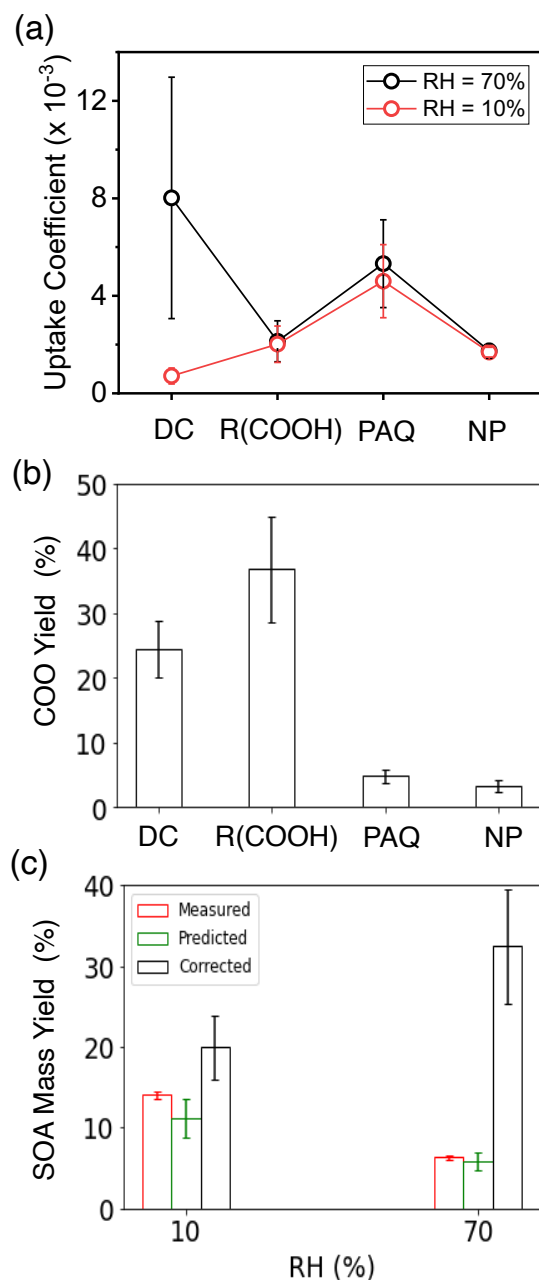
777

778



779

780 **Figure 6.** The effects of NO_x. (a) Time-dependent gas-phase concentrations of 5-methyl-2-
 781 nitrophenol (black, *m/z* = 154), dimethyl nitrophenol (red, *m/z* = 168), and dihydroxy nitrotoluene
 782 (blue, *m/z* = 184). The numbers denote the mass to charge ratio (*m/z*). Initiation of photooxidation
 783 by ultraviolet light occurred at *t* = 0. (b) GF (black) and SSA (red) at 120 min with varying NO_x
 784 concentration from 0 to 500 ppb. (c) Dependence of aerosol-phase relative mass intensities (RI)
 785 for carboxylates (black), oligomers (green), NCO (brown), and nitrophenols (red) on NO_x
 786 concentration for (NH₄)₂SO₄ seed particles with 19 ppb NH₃ at RH = 70%. The error bar denotes
 787 1σ of 3 replicated measurements.



788

789 **Figure 7.** Uptake coefficient, COO yield, and SOA mass yield. (a) Average uptake coefficients (γ)
 790 for different types of COOs at 10% (red) and 70% (black) RH for $(\text{NH}_4)_2\text{SO}_4$ seed particles with
 791 19 ppb NH_3 at 298 K. (b) COO yields: dicarbonyls, organic acids, polyhydroxy aromatics/quinones,
 792 and nitrophenols are represented by DC, $\text{R}(\text{COOH})_n$, PAQ, and NP, respectively. (c) SOA mass
 793 yields at 10% (left columns) and 70% RH (right). The red, green, and black columns represent the
 794 measured, predicted, and corrected (for wall loss) SOA mass yields according to eq. 19-22. All
 795 experiments are carried out for $14 \mu\text{g m}^{-3}$ $(\text{NH}_4)_2\text{SO}_4$ seed particles with 19 ppb NH_3 at 298 K. The
 796 error bars denote the 1σ of 3 replicated measurements or by accounting for error propagation of
 797 the measured parameters.

798

799 **Table 1. Summary of experimental conditions.**

Experiment #	Seed particle	NH ₃ concentration (ppb)	NO _x concentration (ppb)	RH
Exp. 1	AS	19	0	70%
Exp. 2	AS	0	0	70%
Exp. 3	ABS	0	0	70%
Exp. 4	NaCl	0	0	70%
Exp. 5	AS	9.5	0	70%
Exp. 6	AS	28.5	0	70%
Exp. 7	ABS	9.5	0	70%
Exp. 8	ABS	19	0	70%
Exp. 9	ABS	28.5	0	70%
Exp. 10	NaCl	9.5	0	70%
Exp. 11	NaCl	19	0	70%
Exp. 12	NaCl	28.5	0	70%
Exp. 13	AS	19	0	10%
Exp. 14	AS	19	0	30%
Exp. 15	AS	19	0	50%
Exp. 16	AS	19	100	70%
Exp. 17	AS	19	300	70%
Exp. 18	AS	19	500	70%

800

801